Research Article

Journal of Environmental Nanotechnology

# Green Synthesis, Characterization, and Biomedical Applications of *Vernonia elaeagnifolia*-Mediated Magnesium Oxide Nanoparticles

Alagendran Subbarayalu[1], Ramesh Murugesan[2*], Kumar Vimal[3], R. Suresh[4], R. Rasu[5] and K. Manikandan[6]

[1]Department of Research, Saveetha College of Nursing, Saveetha Institute of Medical and Technical Sciences, Saveetha University, Thandalam, Chennai, TN, India
[2]Department of Electrical and Electronics Engineering, M. Kumarasamy College of Engineering, Karur, TN, India
[3]Department of Botany, IIMT University Meerut, Meerut, UP, India
[4]Department of Mechanical Engineering, Vel Tech High Tech Dr. Rangarajan Dr. Sakunthala Engineering College, Tiruvallur, TN, India
[5]Department of Biochemistry, Kongu Arts and Science College, Nanjanapuram, Erode, TN, India
[6]Department of Chemistry, Velalar College of Engineering and Technology, Thindal, Erode, TN, India
Received: 03.07.2026 Accepted: 05.08.2026 Published: 30.09.2026
*rameshr14258@gmail.com

## ABSTRACT

Plant-mediated synthesis of metallic nanoparticles has an attractive green approach owing to its sustainability, low environmental impact, and avoidance of hazardous chemicals associated with traditional preparation techniques. In this investigation, magnesium oxide nanoparticles (MgONPs) were successfully synthesized by aqueous leaf and flower extracts of *Vernonia elaeagnifolia*, which functioned as naturally occurring reducing and capping agents. Nanoparticle generation was first evidenced by immediate change in reaction mixture color and subsequently verified through Fourier-transform infrared spectroscopy, UV–visible spectroscopy, scanning electron microscopy (SEM), X-ray diffraction (XRD), and energy-dispersive X-ray spectroscopy (EDX). The UV–Vis spectra displayed distinct absorption maxima at 285 nm for leaf-extract MgONPs (MgONPsLe) and 291 nm flower-extract MgONPs (MgONPsFl), indicating the formation of nanoparticles. The XRD results confirmed a crystalline face-centered cubic MgO phase crystallite dimensions between 22 and 23 nm. The SEM observations revealed mainly rod-shaped and plate-like particles for both MgONPsLe and MgONPsFl, whereas EDX analysis verified magnesium and oxygen as the predominant elements, with magnesium contents of 29.03 at% and 30.62 at%, respectively. Antibacterial, antioxidant, antibiofilm, and antidiabetic properties of both the plant extracts and the synthesized nanoparticles were systematically investigated. The flower extract produced the greatest antioxidant performance, achieving 82.15% DPPH free-radical scavenging activity and FRAP $IC_{50}$ of 0.812 mg $mL^{-1}$. MgONPsFl exhibited the highest biological effectiveness, showing minimum inhibitory concentration of 37.5–75 µg $mL^{-1}$, biofilm inhibition reaching 64.75%, and strong inhibitory activity against α-glucosidase and α-amylase with $IC_{50}$ values of 22.9 and 20.6 µg $mL^{-1}$. The results demonstrate that *Vernonia elaeagnifolia*-derived MgONPs represent effective bioactive nanomaterials with considerable potential for antimicrobial and biomedical applications, while confirming that plant phytochemicals play a significant role in directing nanoparticle formation, structural characteristics, and biological performance.

**Keywords:** MgO nanoparticles; *Vernonia elaeagnifolia*; Antioxidant activity; Antimicrobial activity; Biofilm inhibition; α-Amylase activity.

## 1. INTRODUCTION

Sustainable nanotechnology based on biological resources has become a highly effective strategy for fabricating metallic and metal oxide nanoparticles. Traditional chemical and physical synthesis routes generally depend on toxic reagents, elevated processing temperatures, substantial energy input, and sophisticated equipment, reducing their environmental sustainability and limiting industrial-scale implementation. Alternatively, plant-assisted fabrication offers a cost-effective, environmentally benign, and biologically compatible approach by exploiting naturally abundant phytoconstituents for nanoparticle reduction, stabilization, and surface protection. Phytochemicals including flavonoids, phenolic compounds, alkaloids, tannins, proteins, and terpenoids, actively promote nanoparticle generation without relying on hazardous chemical additives. As a result, this biosynthetic strategy has gained widespread interest for developing advanced nanomaterials with improved functional and biological properties suitable for biomedical, pharmaceutical, environmental, and agricultural applications (Muhaimin *et al.* 2023). The rapid development of green nanotechnology has also extended beyond metal oxide nanoparticles to other biologically synthesized

nanomaterials. Mycosynthesized silver and selenium nanoparticles have demonstrated excellent antibacterial, antibiofilm, and synergistic antimicrobial activities against multidrug-resistant pathogens, highlighting the versatility of biological synthesis approaches for producing highly effective antimicrobial nanomaterials (Fahmy *et al.* 2025). Likewise, biogenic palladium nanoparticles synthesized using plant extracts exhibited strong antibacterial activity, effective biofilm inhibition, enhanced antibiotic efficacy, and accelerated wound healing, further emphasizing the biomedical significance of environmentally benign nanoparticle synthesis (Hamid *et al.* 2024). Among various metal oxide nanomaterials, magnesium oxide nanoparticles have received significant attention due to their excellent chemical stability, thermal resistance, low toxicity, large specific surface area, and remarkable biological properties. Their unique physicochemical characteristics enable efficient interactions with microbial membranes and reactive oxygen species generation, making MgO nanoparticles effective antimicrobial agents. Furthermore, their excellent biocompatibility has promoted applications in antioxidant therapy, drug delivery, tissue engineering, anti-inflammatory treatment, anticancer therapy, and biosensing.

Several medicinal plants have successfully been employed for the biosynthesis of MgO nanoparticles. MgO nanoparticles synthesized using *Pterocarpus marsupium* heartwood extract exhibited spherical morphology with particle sizes ranging from 13 to 25 nm and demonstrated remarkable antioxidant, antibacterial, anti-inflammatory, and antidiabetic, confirming effectiveness of plant-mediated synthesis in producing multifunctional nanomaterials (Ammulu *et al.* 2021). Similarly, MgO nanoparticles synthesized using *Alstonia scholaris* leaf extract exhibited high crystallinity with an average crystallite size of 19.57 nm. The biosynthesized nanoparticles showed stronger antioxidant and anti-inflammatory activities than the standard antioxidant, suggesting their potential for pharmaceutical and cosmetic applications (Shahid *et al.* 2022). The versatility of green synthesis has also been demonstrated using different medicinal plants. MgO nanoparticles produced from *Phyllanthus emblica* fruit extract exhibited a characteristic UV–Visible absorption peak at 385 nm and showed excellent antioxidant and anti-inflammatory activities, indicating their suitability for large-scale biomedical applications (Behera *et al.* 2021). Likewise, MgO nanoparticles synthesized from *Oryza sativa* grain extract displayed excellent biocompatibility together with significant antioxidant, anti-inflammatory, antidiabetic, and anticancer activities, highlighting the broad therapeutic potential of biosynthesized MgO nanoparticles (Velsankar *et al.* 2023).

Recent investigations have further expanded the range of plant resources used for MgO nanoparticle synthesis. Bioinspired MgO nanoparticles synthesized using *Azadirachta indica* leaf extract demonstrated excellent antioxidant, antibacterial, anti-inflammatory, antidiabetic, and anticancer activities together with remarkable biological stability (Al-Harbi *et al.* 2024). Similarly, MgO nanoparticles synthesized from *Madhuca longifolia* flower extract exhibited a highly pure cubic crystal structure, and optimization studies confirmed that precursor concentration significantly influenced nanoparticle size and antibacterial performance (Kurhade *et al.* 2024). The biological performance of MgO nanoparticles has also been enhanced through alternative medicinal plants. MgO nanoparticles synthesized using *Matricaria chamomilla* extract exhibited quasi-spherical morphology and significant antiplasmodial activity against both chloroquine-sensitive and resistant *Plasmodium falciparum* strains, demonstrating their potential for antimalarial therapy (Farzaneh *et al.* 2025). Likewise, MgO nanoparticles synthesized from *Pterocarpus santalinus* extract exhibited concentration-dependent antibacterial activity against both Gram-positive and Gram-negative bacteria, confirming their broad-spectrum antimicrobial potential (Sahith *et al.* 2025).

Beyond monometallic nanomaterials, hybrid metal oxide nanoparticles have attracted considerable research interest because synergistic interactions between different metal oxides often produce superior physicochemical and biological properties. A green-synthesized ZnO/MgO bimetallic nanocomposite exhibited enhanced antioxidant, antibacterial, antidiabetic, and plant growth-promoting activities compared with individual metal oxides, demonstrating the advantages of combining multiple nanomaterials into a single multifunctional system (Selim *et al.* 2025a). Other multicomponent nanostructures have also demonstrated remarkable biomedical performance. $MnO_2$–MgO bimetallic nanoparticles synthesized using plant extracts exhibited significant antioxidant activity together with strong antimicrobial and antibiofilm properties against pathogenic microorganisms (Elhawary *et al.* 2025). Similarly, $TiO_2$–MgO–Au trimetallic nanoparticles displayed potent antibacterial, antibiofilm, and anticancer activities, indicating that hybrid nanostructures represent an effective strategy for developing multifunctional biomedical nanomaterials (Soliman *et al.* 2025).

Among medicinal plants, *Vernonia elaeagnifolia* has recently gained considerable attention because of its rich phytochemical composition and diverse pharmacological properties. Zinc oxide nanoparticles synthesized using *Vernonia elaeagnifolia* leaf extract exhibited spherical morphology with an average particle size of approximately 45 nm and demonstrated remarkable antioxidant, antibacterial, anticancer, and DNA-binding activities, confirming the capability of this plant to mediate the green synthesis of highly functional nanoparticles (Chandramohan *et al.*

2025). The suitability of *Vernonia elaeagnifolia* for green nanotechnology has been further demonstrated through the biosynthesis of gold nanoparticles. Biosynthesized Au nanoparticles exhibited superior apoptotic activity against glioma cells together with significant antiplatelet effects, highlighting the presence of potent reducing and stabilizing phytochemicals within the plant extract (Sherin *et al.* 2024). Apart from nanoparticle synthesis, *Vernonia elaeagnifolia* itself possesses significant medicinal value. Methanolic extracts of the plant exhibited pronounced antipyretic and hypoglycemic activities without producing irritant effects in experimental models, indicating that the plant contains abundant pharmacologically active secondary metabolites capable of supporting both therapeutic applications and green nanoparticle synthesis (Touqeer *et al.* 2024).

The growing emphasis on sustainable material development is also evident in advanced engineering materials, where eco-friendly processing strategies have significantly improved the mechanical performance of natural biomaterials and hybrid composites. Process optimization has enhanced the mechanical properties of heat-treated date palm seed biomaterials, while cellulose-reinforced natural fiber composites and ceramic-filled hybrid composites have achieved remarkable improvements in strength, fatigue life, impact resistance, and wear behavior, demonstrating the increasing importance of sustainable material design across diverse scientific disciplines (Chowdhury *et al.* 2026; Gupta *et al.* 2026; Subbarao *et al.* 2026).

Although substantial advances have been made in green production of MgO nanoparticles using wide range of medicinal plants, the application of *Vernonia elaeagnifolia* has received comparatively little attention. Previous research involving this medicinal species has mainly concentrated on the synthesis of ZnO and Au nanoparticles, while its capability for fabricating MgO nanoparticles remains largely unexplored. In addition, a detailed comparative investigation of MgO nanoparticles prepared from different plant organs, especially leaf and flower extracts, has not been conducted to clarify the effects of phytochemical variation on nanoparticle synthesis, morphology, crystallinity, antioxidant potential, antibacterial properties, and antibiofilm activity. Accordingly, this work focuses on green fabrication of MgO nanoparticles by aqueous extracts obtained from the flowers and leaves of *Vernonia elaeagnifolia* by straightforward, sustainable, and eco-conscious process. Prepared nanoparticles were thoroughly examined by UV–Visible spectroscopy, X-ray diffraction (XRD), Fourier-transform infrared spectroscopy (FTIR), Scanning Electron Microscopy (SEM), and X-ray spectroscopy (EDX) to evaluate their optical, crystalline, morphological, and elemental characteristics. In addition, antioxidant, antibacterial, and antibiofilm performances were comprehensively investigated to determine how the selected plant part influences nanoparticle features and biological effectiveness. The findings offer valuable evidence supporting the use of *Vernonia elaeagnifolia* as a renewable source for the green fabrication of MgO nanoparticles and highlight its promise for producing multifunctional bioactive nanomaterials with prospective biomedical applications.

## 2. MATERIALS AND METHODS

### 2.1 Preparation of Plant Extracts

*Vernonia elaeagnifolia* leaves were harvested from foothill region of Sathyamangalam Tiger Reserve in Erode District, Tamil Nadu, India, between March and April 2024. Separate portions of 20 g of dried leaf and flower powders were transferred into individual beakers, followed by the addition of 100 mL of deionized water. The suspensions were incubated at 37 °C for 1 day to facilitate the extraction of bioactive constituents. After incubation, each extract was passed through filter paper, and the filtrates were preserved at 4 °C under dark conditions for biosynthesis of magnesium oxide nanoparticles.

### 2.2 Green Synthesis of MgO Nanoparticles

MgO nanoparticles were biosynthesized by aqueous leaf extract of *Vernonia elaeagnifolia* through a modified plant extract-mediated precipitation technique (Wulandari *et al.* 2024). In brief, fresh 0.1 M aqueous solution of magnesium nitrate hexahydrate [$Mg(NO_3)_2 \cdot 6H_2O$] was prepared by dissolving analytical-grade magnesium nitrate in distilled water (Kongara *et al.* 2025). For MgO nanoparticle preparation, 20 mL of *Vernonia elaeagnifolia* leaf extract was introduced slowly into 100 mL of the magnesium nitrate solution while maintaining constant magnetic agitation. The reaction suspension was kept at 70 ± 2 °C for 2 hours, during which a creamy-white precipitate developed, confirming the synthesis of the magnesium precursor mediated by plant-derived phytochemicals. Precipitate was recovered by centrifugation at 10,000 rpm for 15 minutes, rinsed three times with deionized water and subsequently with ethanol to eliminate residual biomolecules and other contaminants, and then oven-dried at 80 °C for 12 hours. The dried material was calcined at 500 °C for 3 hours to produce crystalline MgO nanoparticles, which were utilized for subsequent characterization and biological evaluation.

### 2.3 Physicochemical Characterization of MgONPs

Synthesized samples were analyzed by UV–Visible spectroscopy, XRD, and FTIR. Formation of magnesium oxide nanoparticles was verified by UV–Visible spectral analysis employing deionized water as

the reference blank. Spectral analysis was performed by UNICO 2080 spectrophotometer within the wavelength range 220–600 nm (Devi and Ramesh, 2026), which encompasses the characteristic ultraviolet and visible absorption regions of both organic and inorganic compounds. The instrument was operated at a scanning rate of 1–2 nm/min with baseline correction against the blank, and all measurements were recorded at ambient temperature (20–25 °C). The FTIR spectra were obtained on a FTIR 640 spectrometer over the range 4000–400 $cm^{-1}$ using KBr pellet method. Spectral acquisition were carried out at resolution of 4 $cm^{-1}$ with 32 accumulated scans under ambient conditions (Mustafa *et al.* 2021). Crystalline phase analysis was performed using D8 ADVANCE BRUKER X-ray diffractometer. Diffraction profiles were collected across 2θ interval of 10–80° at scan rate of 0.5–2°/min.

The surface architecture, elemental distribution of magnesium oxide nanoparticles (MgONPs) synthesized from the flower (MgONPsFl) and leaf (MgONPsLe) of *Vernonia elaeagnifolia* were investigated using a Zeiss Gemini Scanning Electron Microscope (SEM) coupled with energy-dispersive X-ray analysis system.

## 2.4 Bioactivities of Plant Extracts and MgONPs

### 2.4.1 Antioxidant Performance Evaluation

#### *2.4.1.1 DPPH Antioxidant Assay*

The free radical scavenging of extracts was analysed by 2,2-diphenyl-1-picrylhydrazyl (DPPH) (Govindhraj and Shanmugam, 2025). About 20 µL of test specimen was mixed with 200 µL of 120 µM DPPH solution prepared in 96% methanol. The mixture was allowed to react for 30 minutes under dark conditions at ambient temperature. Following incubation, absorbance was recorded at 517 nm by microplate spectrophotometer. Free radical scavenging activity was calculated as percentage inhibition (%) in comparison with the negative control.

#### *2.4.1.2 FRAP Antioxidant Assay*

Ferric reducing antioxidant capacity of specimens was assessed as follows. Briefly, 50 µL of each specimen was mixed with 50 µL of 1% potassium ferricyanide [$K_3Fe(CN)_6$] and 50 µL of deionized water. The reaction mixture was maintained at 45 °C for 15 minutes. Thereafter, 50 µL of trichloroacetic acid together with 10 µL of $FeCl_3$ was introduced, followed by an additional incubation at 50 °C for 10 minutes. Absorbance was subsequently recorded at 700 nm by Multiskan microplate spectrophotometer. Greater absorbance values corresponded to stronger ferric ion reducing ability, indicating the conversion of $Fe^{3+}$ to $Fe^{2+}$ by the antioxidant compounds present in the samples. Butylated hydroxytoluene was employed as the standard antioxidant.

### 2.4.2 Antioxidant Activity Evaluation

The assay measures antioxidant capacity through the conversion of Mo(VI) to (V) by test specimen, followed by generation of green phosphate under acidic conditions(Ali *et al.* 2024). About 0.1 mL of the sample was added to 1 mL of the reagent containing 28 mM sodium phosphate, 4 mM ammonium molybdate and 0.6 M sulfuric acid. The reaction mixture was heated at 95 °C for 90 minutes and then allowed to cool to room temperature. Absorbance was subsequently recorded at 695 nm using reagent blank as the reference.

### 2.4.3 Anti-Inflammatory Bioactivity Assessment

The aqueous extracts from flowers and leaves, along with corresponding MgONPs were assessed. This involves assessing their capacity to prevent denaturation of BSA following the incubation of mixture at 36 °C for 20 minutes. Absorbance was assessed at 660 nm to evaluate the extent of percentage inhibition and protein denaturation. *I*(%) was computed according to equation (1) as follows (Kandavalli *et al.* 2025):

$$I\% = 100 \times \left(\frac{Ac - As}{Ac}\right) \quad \ldots (1)$$

### 2.4.4 Antidiabetic Bioactivity Assessment

Antidiabetic activity of prepared magnesium oxide nanoparticles was investigated by evaluation of their suppressive effect on α-glucosidase and α-amylase enzymes. For the α-amylase assay, 500 µL of MgONPs dispersion at various concentrations was blended with 500 µL of α-amylase. The mixture was maintained at 20 °C for 15 minutes before introducing 500 µL of 1% starch. Enzyme activity was terminated using 1 mL 3,5-dinitrosalicylic acid solution, followed by heating on a water bath for 4 minutes. After cooling under ambient conditions, 5 mL of deionized water was added and the optical density was determined at 540 nm. Acarbose was employed as standard reference inhibitor. Percentage of α-amylase suppression was subsequently determined.

### 2.4.5 Antimicrobial Activity

#### *2.4.5.1 Zone of Inhibition Assay*

Antimicrobial potential of test materials was investigated using *Candida krusei* ATCC 6258, *Candida albicans* ATCC 90028, *Bacillus cereus* ATCC 14579, *Enterococcus faecalis* ATCC 29212, *Salmonella typhimurium* ATCC 14028, *Staphylococcus epidermidis* CIP 106510, *Staphylococcus aureus* ATCC 43300, *Listeria monocytogenes* ATCC 19115, and *Escherichia coli* ATCC 35218. Their inhibitory effects against the microbial species were determined by employing agar well diffusion assay (Amina *et al.* 2020). The bacterial

inoculum was standardized to $10^7$ CFU/mL, whereas *Candida* inoculum was standardized to $10^6$ spores/mL. Antibacterial evaluation was carried out using Mueller–Hinton agar, while Sabouraud chloramphenicol agar was selected for antifungal assessment. All inoculated plates were maintained at 36 °C for 1 day. Every experiment was performed three times to ensure reproducibility. Amphotericin B (25 µg $mL^{-1}$) and levofloxacin (5 µg) were included as reference antimicrobial agents.

#### *2.4.5.2 Minimum Bactericidal Concentration (MBC) and Minimum Inhibitory Concentration (MIC) Assessment*

The MBC of magnesium oxide nanoparticles was determined through a broth dilution assay performed at sterile 96-well microtiter plates with flat bottoms. For the determination of MBC, 10 µL aliquots collected from wells with no detectable growth was streaked onto agar media and incubated for 1 day. Recovery of bacterial colonies show bacteriostatic response, whereas absence of colony development confirm bactericidal concentration of synthesized magnesium oxide nanoparticles. The minimum inhibitory concentration (MIC) of MgONPsFl and MgONPsLe against the tested bacterial strains was determined using the broth microdilution method in sterile flat-bottom 96-well microtiter plates. Two-fold serial dilutions of each MgONP suspension were prepared in Mueller–Hinton broth to obtain concentrations of 18.75, 37.5, 75, 150, and 300 µg $mL^{-1}$. Each well was inoculated with the standardized bacterial suspension. Inoculated broth without MgONPs served as the growth control, whereas uninoculated broth was maintained as the sterility control. The microplates were incubated at 36 °C for 24 h, and the MIC was defined as the lowest concentration of MgONPs showing no visible microbial growth compared with the growth control. Wells exhibiting no detectable growth were subsequently used for determination of the minimum bactericidal concentration (MBC).

#### *2.4.5.3 Biofilm Inhibitory Activity*

The influence of the synthesized magnesium oxide nanoparticles on microbial biofilm development was investigated using sterile 96 flat-bottom microtiter plates.

#### *2.4.5.4 Effect of MgONPs on Bacterial Cell Wall*

*Staphylococcus aureus* and *Bacillus cereus* cultures were grown on solid agar at 37 °C for 1 day. The harvested cells were washed with deionized water and subsequently dispersed in 50 mM phosphate buffer. Then, 100 µL of bacterial cell wall suspension was transferred into an Eppendorf tube containing 50 µL of test sample. The mixture was maintained at 37 °C for 1 hour. Lysozyme-like activity was determined in arbitrary units by monitoring the decline in absorbance.

#### 2.4.6 Lipopolysaccharide Degradation

Ability of synthesized magnesium oxide nanoparticles to promote lipopolysaccharide degradation was investigated. Gram-negative bacterial cultures were grown at 1 mL of Luria-Bertani medium containing either MgONPs (150 µg/mL) or no nanoparticles at 36 °C for 18 hours with continuous agitation. Equal range of 5% phenol reagent was then added, followed immediately by fivefold sulfuric acid. The resulting mixture was kept in dark for 1 hour, after which absorbance was determined at 490 nm to evaluate the extent of lipopolysaccharide (LPS) degradation.

### 2.5 Statistical Analysis

Experimental findings are given as mean ± standard error. Statistical differences among groups was evaluated by Student–Newman–Keuls (SNK) multiple comparison procedure with level of significance established at $p < 0.05$. Data points assigned an identical superscript letter did not differ significantly.

## 3. RESULTS AND DISCUSSION

### 3.1 Green-synthesized MgO Nanoparticles: Structural Characterization

#### 3.1.1 UV-visible Analysis

Formation of MgONPs was confirmed by the distinct visual transformation of reaction solution from light yellow to dark brown. Observation indicates conversion of $Mg^{2+}$ ions into MgONPs (Fig. 1).

Successful formation of magnesium oxide nanoparticles was additionally verified by UV–Vis spectroscopy, which exhibited characteristic absorption maxima at 285 nm for the leaf-extracted MgONPs and 291 nm for the flower-extracted MgONPs. A previous investigation reported green production of MgO nanoparticles by *Acalypha indica* leaf extract, where UV–Vis analysis revealed a characteristic band at 284 nm and XRD measurements indicated an average crystallite size of 10 nm (Ramaprabha *et al.* 2025).

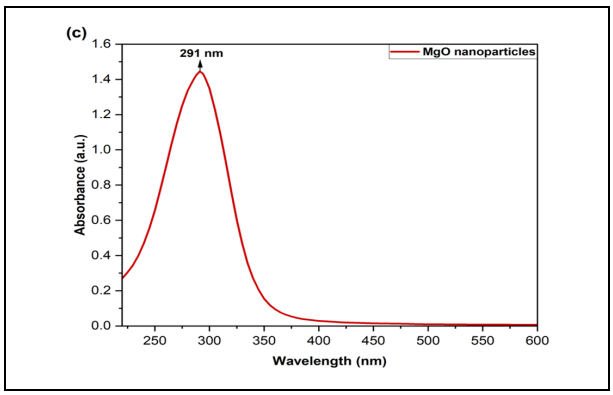

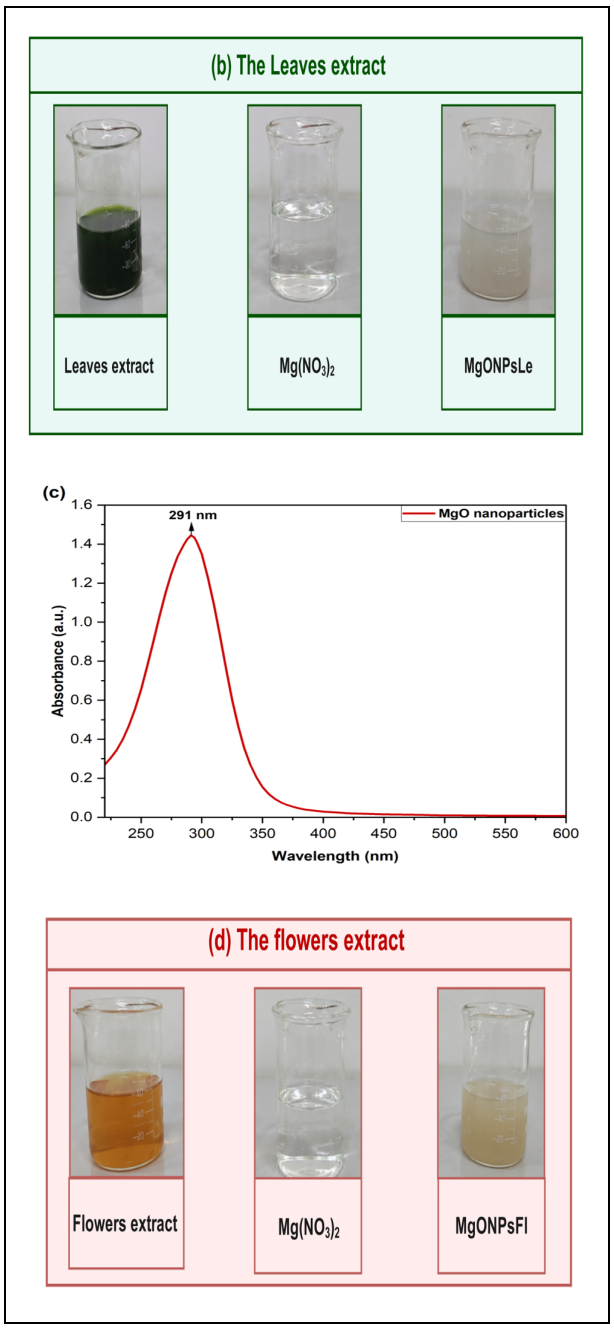


**Fig. 1: (a) Optical absorbance profile of MgONPsLe, (b) Leaves extract and MgONPsLe, (c) Optical absorbance profile of MgONPsFl and (d) Photographs of flower extract and MgONPsFl**

### 3.1.2 Fourier Transform Infrared Analysis

The FTIR profiles (Fig. 2a&b) revealed the functional groups associated with the leaf and flower extracts as well as their respective synthesized nanoparticles, demonstrating the effective biomediated conversion and subsequent stabilization of the nanomaterials.

Fig. 2(a) illustrates the FTIR spectra of the leaf extract and the MgO nanoparticles prepared from the same extract, highlighting the involvement of plant-derived biomolecules in nanoparticle synthesis. The spectrum of leaf extract exhibits broad peak at 3398 $cm^{-1}$, characteristic of O–H stretching vibrations originating from phenolics, flavonoids, and alcoholic constituents. Signals detected at 2923 and 2853 $cm^{-1}$ are associated with asymmetric and symmetric stretching modes of aliphatic C–H bonds. The peak centered at 1734 $cm^{-1}$ is characteristic of carbonyl (C=O) stretching from ester and carboxylic acid functionalities, whereas the absorption at 1636 $cm^{-1}$ is related to the amide I region arising from C=C/C=O vibrations. Furthermore, the peaks at 1517, 1452, and 1383 $cm^{-1}$ correspond to aromatic ring C=C stretching, $CH_2$ deformation, and C–N stretching together with $CH_2$ bending, respectively. The peaks appearing at 1246, 1072, and 1030 $cm^{-1}$ are assigned to C–O stretching of phenolic compounds, alcohols, and polysaccharides, while the peaks at 874 and 652 $cm^{-1}$ are attributed to aromatic C–H and out-of-plane deformation modes.

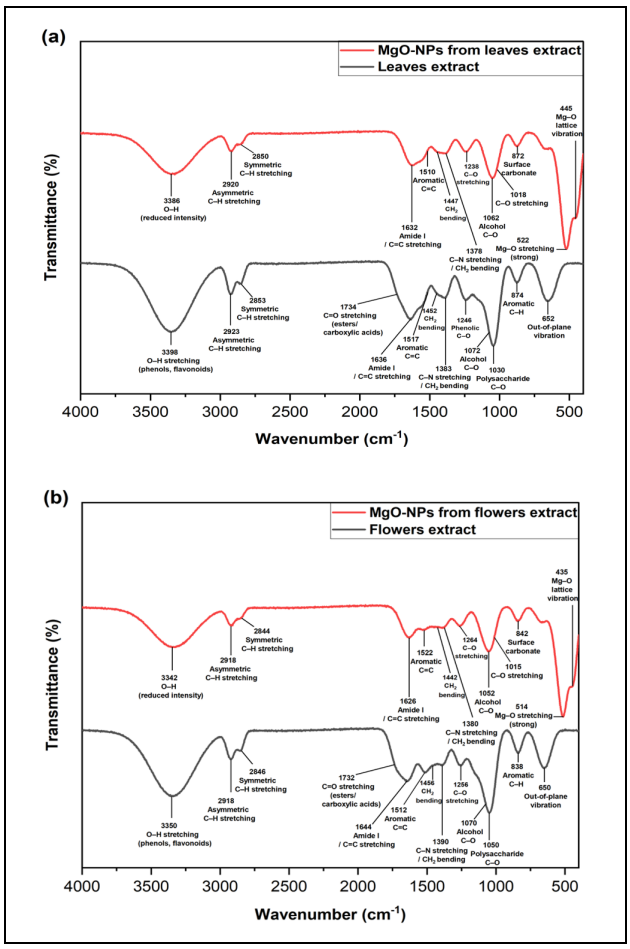


**Fig. 2: (a) FTIR profiles: leaf extract, MgONPsLe and (b) FTIR profiles: flower extract, MgONPsFl**

After the production of MgO nanoparticles, the broad O–H peak shifted to 3386 $cm^{-1}$ and exhibited lower intensity, whereas the aliphatic C–H stretching signals were detected at 2920 and 2850 $cm^{-1}$. The amide I peak

was shifted to 1632 $cm^{-1}$, while the peaks corresponding to aromatic C=C stretching, $CH_2$ deformation, phenolic C–O, alcoholic C–O, and polysaccharide C–O vibrations were identified at 1510, 1447, 1238, 1062, and 1018 $cm^{-1}$, respectively. A weak peak at 872 $cm^{-1}$ was associated with carbonate species adsorbed on the nanoparticle surface. In addition, prominent peaks located at 522 and 445 $cm^{-1}$ were characteristic of Mg–O bond stretching and Mg–O lattice vibrational modes, respectively, thereby verifying the successful crystallization of MgO nanoparticles.

Fig. 2(b) depicts the FTIR profiles of the flower extract and the MgO nanoparticles obtained from the flower extract. The spectrum of the flower extract displays a broad peak centered at 3350 $cm^{-1}$, corresponding to O–H stretching vibrations arising from hydroxyl-containing phytoconstituents, including phenolic compounds and flavonoids. The aliphatic C–H asymmetric and symmetric stretching modes are observed at 2918 and 2846 $cm^{-1}$, respectively, whereas the peak at 1732 $cm^{-1}$ is characteristic of carbonyl (C=O) stretching associated with ester and carboxylic acid groups. The signal appearing at 1644 $cm^{-1}$ is assigned to the amide I region resulting from C=C/C=O vibrations. Moreover, the peaks located at 1512, 1456, and 1390 $cm^{-1}$ are attributed to aromatic ring C=C stretching, $CH_2$ deformation, and C–N stretching together with $CH_2$ bending, respectively. The peaks at 1256, 1070, and 1050 $cm^{-1}$ correspond to C–O stretching of phenolic compounds, alcohols, and polysaccharides, while the peaks at 838 and 650 $cm^{-1}$ are assigned to aromatic C–H and out-of-plane deformation vibrations.

Upon formation of the MgO nanoparticles, the broad O–H absorption was displaced slightly to 3342 $cm^{-1}$, whereas the aliphatic C–H stretching features were retained at 2918 and 2844 $cm^{-1}$ with lower absorbance. The amide I signal was observed at 1626 $cm^{-1}$[1], while the absorptions located at 1522, 1442, 1380, 1264, 1052, and 1015 $cm^{-1}$ confirmed the persistence of aromatic, phenolic, and alcoholic functionalities on the nanoparticle surface. A minor absorption centered at 842 $cm^{-1}$ was assigned to adsorbed carbonate species. Additionally, the pronounced bands detected at 514 and 435 $cm^{-1}$ correspond to Mg–O bond stretching and Mg–O lattice vibrational modes, respectively, thereby verifying the successful production of crystalline MgO nanoparticles.

A comparative evaluation of the spectra recorded prior to and following nanoparticle generation reveals that both leaf and flower extracts possess prominent amide absorptions and O–H, C=O, indicating phytoconstituents involved in the conversion process.

In contrast, the spectra of the flower-derived and leaf-derived nanoparticles display minor displacements of C=O, O–H and amide absorption. The change in intensity suggest adsorption of phytomolecules onto the nanoparticles, resulting in stabilization of formed nanostructures. The observed spectral shifts further demonstrate the association of metal ions with the corresponding functional groups.

The suggested eco-friendly synthesis pathway proceeds through four sequential stages. The initial stage involves electron transfer, during which phenolic hydroxyl and carbonyl functionalities act as electron donors through the following reaction (1):

$$M^{n+} + \text{phytochemicals} \rightarrow M^{0}\ \text{(nanoparticles)} \ldots (2)$$

These findings indicate that flavonoids and polyphenolic constituents promote metal ion conversion through electron donation, whereas proteins contribute to electron transport. The subsequent stage involves nucleus initiation, in which the newly generated metal species cluster to produce primary nuclei. This is followed by particle development, where the expansion of the nuclei is regulated and biomolecular components govern nanoparticle dimensions. The final stage consists of surface passivation, in which proteins, polyphenolic compounds, and polysaccharides adsorb onto nanoparticle exterior by coordination interactions, hydrogen bonding, and electrostatic attraction. This protective layer suppresses particle aggregation, surface oxidation, and excessive crystal growth. The FTIR analysis further demonstrates that phenolic and flavonoid hydroxyl groups function as electron donors, proteins containing amide I and II peaks provide surface protection, carbonyl functionalities coordinate with the metal surface, and polysaccharides impart steric shielding. The spectral shifts observed for the flower-derived and leaf-derived nanoparticles verify the direct participation of these phytoconstituents in nanoparticle generation and stabilization, confirming an environmentally benign synthesis pathway in which plant-derived biomolecules perform both reducing and stabilizing functions.

#### 3.1.3 X-ray Diffraction Analysis

The crystalline nature of the synthesized nanoparticles was examined using X-ray diffraction analysis. As illustrated in Fig. 3(a), the diffraction profile of the leaf-derived sample exhibits a series of well-defined Bragg reflections characteristic of crystalline MgO. These reflections are indexed to the face-centered cubic (fcc) phase of magnesium oxide nanoparticles. Prominent diffraction maxima are observed at 36.92°, 42.90°, 62.26°, 74.68°, and 78.60°, corresponding to the (111), (200), (220), (311), and (222) lattice planes, respectively. Among these, the intense reflection at 42.90° assigned to the (200) plane signifies the excellent crystalline quality of the biosynthesized MgO nanostructures. In addition, a broad diffuse peak extending from approximately 15° to 35° is evident,

indicating the existence of amorphous organic constituents. Such a halo is commonly associated with plant-mediated synthesis because residual phytochemicals remain attached to the nanoparticle surface. These naturally occurring compounds, including polyphenols, proteins, flavonoids, and polysaccharides, participate in $Mg^{2+}$ conversion and subsequently serve as surface-stabilizing species. Owing to their non-crystalline nature, these organic molecules are responsible for the diffuse amorphous background observed in the XRD pattern.

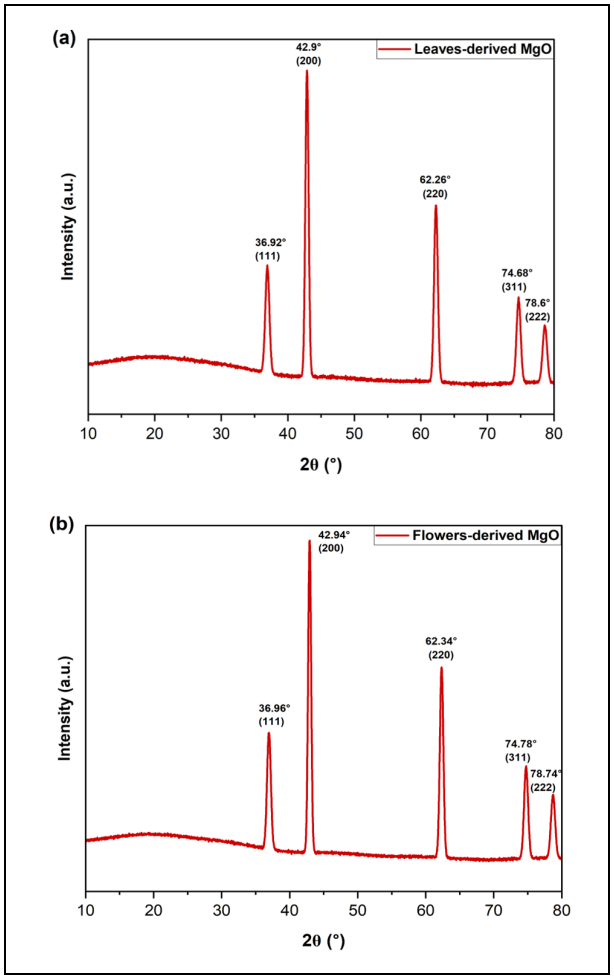


**Fig. 3: (a) XRD pattern of MgONPsLe, (b) XRD pattern of MgONPsFl**

The crystal characteristics of the flower-derived sample were investigated by X-ray diffraction analysis (Fig. 3b). The diffraction profile verifies the successful production of crystalline magnesium oxide nanoparticles using the flower extract as the biogenic source. Distinct Bragg reflections located at 36.96°, 42.94°, 62.34°, 74.78°, and 78.74° are indexed to the (111), (200), (220), (311), and (222) lattice planes, respectively, confirming the fcc phase of MgO. The pronounced reflection associated with the (200) plane reflects the high crystalline quality of the obtained nanoparticles. In addition, a broad diffuse band extending from approximately 15° to 35° is visible, indicating the presence of amorphous phytochemical residues derived from the flower extract. These plant-derived constituents remain adsorbed on the nanoparticle surface following synthesis, where they function as naturally occurring capping and stabilizing molecules.

The XRD profile displays a broad diffuse feature, indicating the existence of non-crystalline organic constituents, a characteristic commonly observed in plant-mediated synthesis. This amorphous fraction is derived from phytoconstituents such as polyphenols, flavonoids, terpenoids and proteins in the leaf extract. The naturally occurring compounds facilitate the transformation of $Mg^{2+}$ into MgO, provide a protective surface layer, and introduce functional groups onto the nanoparticle surface. Consequently, the diffuse halo represents the organic shell enveloping the nanoparticles rather than contamination. Although this amorphous contribution is evident, the well-defined diffraction reflections verify that the nanoparticles retain a highly crystalline MgO core.

The average crystallite dimension was estimated using the Scherrer equation, as expressed in Eq. (2):

$$d = \frac{k \cdot \lambda}{\beta \cos \theta} \quad \ldots (3)$$

### 3.1.4 Scanning Electron Microscopy

Surface morphology was examined using a Zeiss Gemini Scanning electron microscope, and the micrographs (Fig. 4) demonstrate distinct structural characteristics of the biosynthesized nanoparticles. The leaf-derived MgO nanoparticles (MgONPs Le) display compact nanoflake- and rod-like architectures with random alignment, producing a continuous network of clustered structures (Fig. 4a).

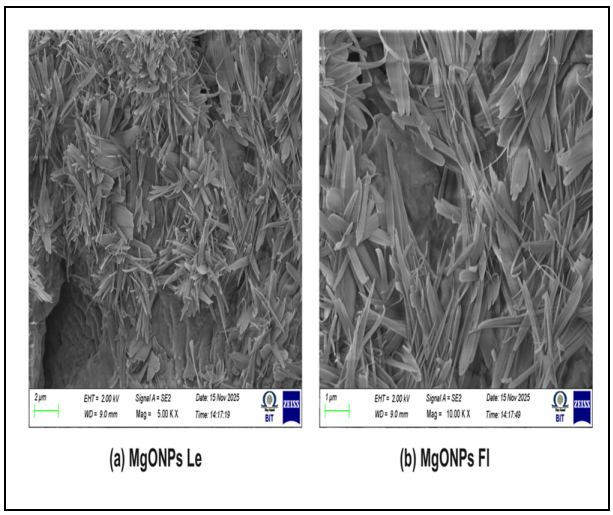


**Fig. 4: (a) SEM Micrograph of MgONPsLe and (b) SEM micrograph of MgONPsFl**

In comparison, the flower-derived MgO nanoparticles (MgONPsFl) are mainly composed of elongated rod-shaped and platelet-like nanostructures with a more homogeneous particle distribution than the leaf-derived counterpart (Fig. 4b). Both materials exhibit clustered particles, which can be attributed to their elevated surface energy together with van der Waals and magnetic interactions occurring during the drying process. The observed differences in morphology and aggregation behavior are most likely related to the distinct phytochemical profiles of the flower and leaf extracts, which govern nanoparticle nucleation, crystal development, and surface stabilization. Collectively, the SEM micrographs verify the formation of MgO nanostructures with irregular rod and platelet-like features, while the morphological variations between the two samples demonstrate the effect of the plant source employed in the green synthesis process.

#### 3.1.5 Elemental Analysis

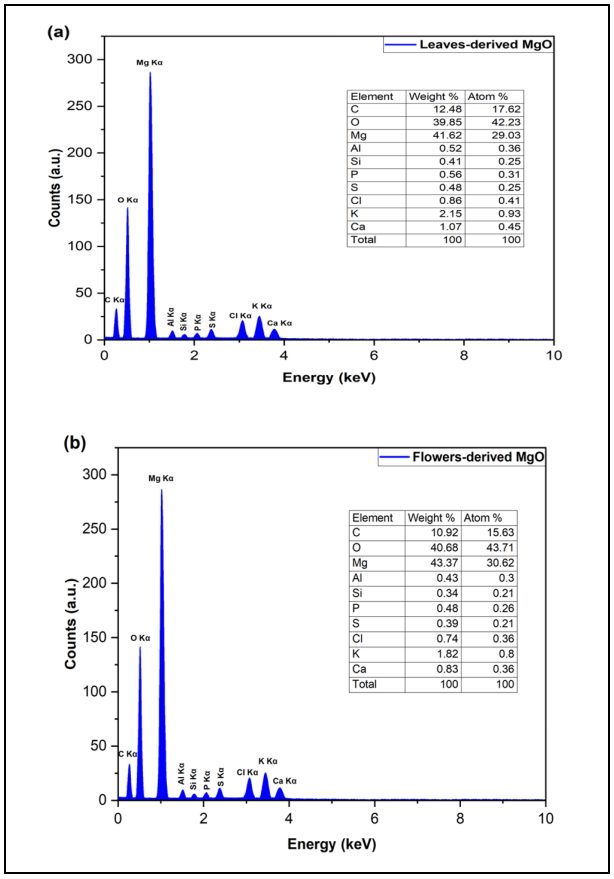


**Fig. 5: (a) EDX spectrum of MgONPsLe and (b) EDX spectrum of MgONPsFl**

Energy-dispersive X-ray spectroscopy characterization of the leaf- and flower-derived MgONPs exhibited an intense characteristic MgO signal near 3 keV, verifying the successful production and elemental composition of the synthesized nanomaterials. The EDX spectra of both samples identified identical elemental constituents, namely C, O, Mg, Al, Si, P, S, Cl, K, and Ca. These constituents are attributed to phytochemicals released from the plant matrix during aqueous extraction. Carbon- and oxygen-containing species function as naturally occurring reducing and surface-stabilizing components, whereas oxygen is associated with the oxide framework of MgO nanoparticles. Sulfur is presumed to originate from sulfur-bearing amino acids and related plant metabolites, which may also assist in nanoparticle stabilization (Fig. 5 a, b).

The elemental distribution expressed as atomic percentage (Atom%) demonstrates measurable differences between the two biosynthesized nanoparticle samples. The MgONPs Fl exhibit a greater magnesium concentration (30.62 Atom%; 43.37 wt%) than the leaf-derived MgONPs (29.03 Atom%; 41.62 wt%). In contrast, the carbon proportion is lower in MgONPsFl at 15.63 Atom% (10.92 wt%) compared with 17.62 Atom% (12.48 wt%) for MgONPsLe. Oxygen accounts for 43.71 Atom% (40.68 wt%) in MgONPs Fl and 42.23 Atom% (39.85 wt%) in MgONPs Le. Moreover, the leaf-derived nanoparticles possess marginally higher levels of Al (0.52 wt%), Si (0.41 wt%), P (0.56 wt%), S (0.48 wt%), Cl (0.86 wt%), K (2.15 wt%), and Ca (1.07 wt%) than the flower-derived sample, which contains Al (0.43 wt%), Si (0.34 wt%), P (0.48 wt%), S (0.39 wt%), Cl (0.74 wt%), K (1.82 wt%), and Ca (0.83 wt%). Such variations in elemental abundance are expected to influence the physicochemical characteristics and biological performance of the prepared MgO nanoparticles.

## 3.2 Biological Activities of MgONPs

#### 3.2.1 Antioxidant Capacity

The flower extract (82.15%) and leaf extract (67.48%) reflect the abundance of phenolic constituents and flavonoids. By comparison, the flower-derived MgO nanoparticles (55.36%) and leaf-derived MgONPs (48.92%) displayed reduced DPPH scavenging efficiency, probably because a portion of the phytoconstituents was utilized or immobilized on the nanoparticle surface during the biosynthesis. Evaluation by the FRAP method showed that the flower extract possessed the greatest ferric ion reducing ability among the plant-based samples ($IC_{50}$ = 0.812 mg $mL^{-1}$), followed by MgONPsFl (1.486 mg $mL^{-1}$), MgONPsLe (2.126 mg $mL^{-1}$), and the leaf extract (2.684 mg $mL^{-1}$). Smaller $IC_{50}$ values represent stronger reducing performance, indicating that the biosynthesized MgONPs preserved considerable electron-transfer capability. with flower extract recording maximum value (1.94 mg (ascorbic acid equivalents) AAE $g^{-1}$MS), followed by leaf extract (1.61 mg AAE $g^{-1}$ MS), MgONPsFl (1.46 mg AAE $g^{-1}$MS), and MgONPsLe (1.34 mg AAE $g^{-1}$ MS) (Table 1). Sharmila and Selvaraj, (2024) reported that MgO nanoparticles prepared from *Scutia myrtina* exhibited 87.68% DPPH radical

scavenging activity, 95.8% anti-inflammatory activity, 85.32% photocatalytic degradation efficiency, and an A549 cytotoxicity $IC_{50}$ of 44.9 µg/mL, highlighting their broad biomedical and environmental potential. The obtained results indicate that nanoparticle production caused a modest decline in antioxidant performance relative to the original plant extracts; however, the biosynthesized MgONPs preserved substantial antioxidant potential due to the surface-associated phytoconstituents. Association between phytochemical abundance and antioxidant capacity were supported by strong positive linear relationship between DPPH radical scavenging activity and total phenolic content (Fig. 6).

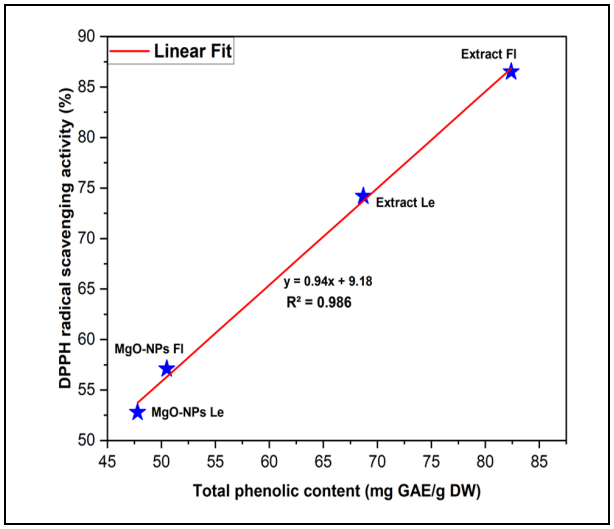


**Fig. 6: TPC–DPPH correlation analysis**

**Table 1. Comparative antioxidant activity**

| | DPPH (PI%) | TAA mg A asc/g MS | FRAP ( $IC_{50}$ mg/ mL ) |
|---|---|---|---|
| Extract Le | 67.48 ± 0.86 | 1.61 ± 0.10 | 2.684 ± 0.16 |
| Extract FI | 82.15 ± 2.18 | 1.94 ± 0.11 | 0.812 ± 0.04 |
| MgONPsLe | 48.92 ± 1.74 | 1.34 ± 0.06 | 2.126 ± 0.12 |
| MgONPsFI | 55.36 ± 2.42 | 1.46 ± 0.07 | 1.486 ± 0.08 |
| Ascorbic acid* (5mg/mL) | 93.42 ± 0.04 | * | * |
| BHT | * | " | 0.574 ± 0.005 |

Collectively, the outcomes suggest that nanoparticle morphology plays major role in determining antioxidant behavior. The flower-derived spherical MgONPs exhibited superior free-radical neutralization in the DPPH assay, whereas the leaf-derived cubic MgONPs showed greater ferric ion reducing capability in the FRAP assay but may display lower stability under specific conditions, thereby influencing their overall antioxidant capacity.

### 3.2.2 Anti-Inflammatory Bioactivity Evaluation

Protein denaturation is a well-recognized event during inflammatory responses, and compounds capable of suppressing this process are regarded as potential anti-inflammatory agents. Accordingly, inhibition of bovine serum albumin (BSA) by test samples were used to evaluate their anti-inflammatory properties. In *in vitro* BSA assay, the flower and leaf extracts produced moderate inhibition values of 19.28% and 15.12%, respectively. By comparison, the corresponding magnesium oxide nanoparticles, MgONPsFl and MgONPsLe, demonstrated markedly greater anti-inflammatory efficacy, achieving inhibition percentages of 43.72% and 37.41%, respectively (Fig. 7).

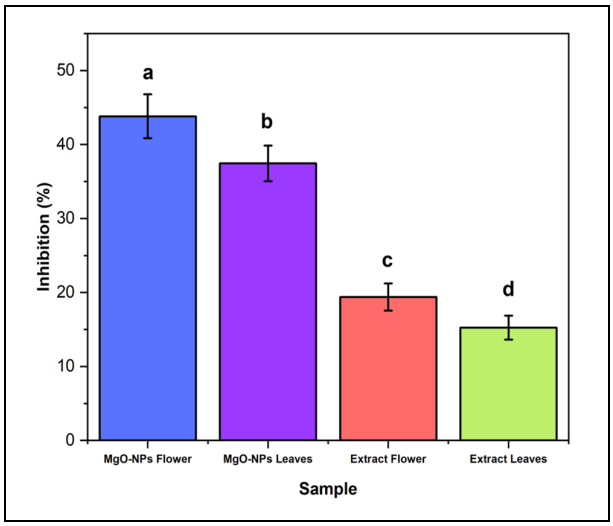


**Fig. 7: Anti-Inflammatory activity assessment**

Phytochemical screening revealed that *Vernonia elaeagnifolia* contains abundant tannins, flavonoids, and polyphenolic constituents, which are responsible for its pronounced antioxidant and anti-inflammatory activities.

### 3.2.3 In Vitro Antidiabetic Enzyme Inhibition

Diabetes remains one of significant health concerns worldwide in the twenty-first century. A key therapeutic approach for treatment of type 2 diabetes mellitus is to slow intestinal glucose uptake by limiting carbohydrate breakdown through suppression of starch-degrading enzymes, including α-glucosidase and α-amylase, thereby reducing postprandial blood glucose levels. Although pharmacological agents such as acarbose, miglitol, and voglibose are widely used for this purpose, their clinical application is frequently limited by

adverse effects. Therefore, this investigation explored MgONPs biosynthesized from the leaf and flower extracts of *Vernonia elaeagnifolia* as plant-based enzyme inhibitors for diabetes management. The starch agar plate assay demonstrated that flower-derived MgO nanoparticles completely suppressed α-amylase activity (Fig. 8), whereas acarbose and leaf-derived MgO nanoparticles exhibited comparatively lower inhibitory responses (Table 2).

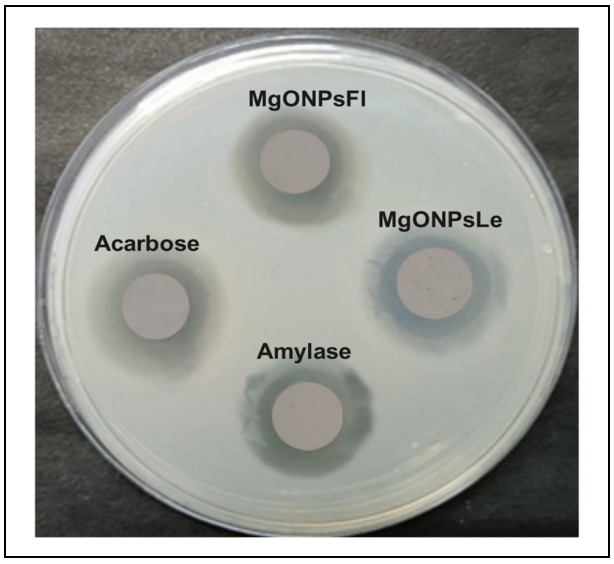


**Fig. 8: Comparative α-Amylase inhibition assay**

**Table 2. α-Amylase Inhibitory Activity**

| Enzyme Inhibition | Inhibition Activity (%) | Diameter Zone (mm) |
|---|---|---|
| Enzyme (alone) | $0.00 \pm 0.00$ | $30 \pm 0.0$ |
| Acarbose (40$\mu$ g) | $13.33 \pm 4.71$ | $26.0 \pm 1.4$ |
| MgONPsFl (30$\mu$ g) | $20.67 \pm 2.36$ | $23.8 \pm 0.8$ |
| MgONPsLe ( 40$\mu$ g ) | $18.33 \pm 2.36$ | $24.5 \pm 0.7$ |

Both MgONPsFl and MgONPsLe exhibited concentration-dependent suppression of α-glucosidase and α-amylase activities. Enzyme inhibition increased steadily as nanoparticle concentration was raised from 5 to 40 µg mL$^{-1}$. At highest test concentration (40 µg mL$^{-1}$), α-amylase inhibition reached 92.1%, 86.5%, and 72.3% for acarbose, MgONPsFl, and MgONPsLe, respectively. Likewise, α-glucosidase inhibition at 40 µg mL$^{-1}$ attained 89.2%, 81.4%, and 67.6% for acarbose, MgONPsFl, and MgONPsLe, respectively. These outcomes indicate that flower-derived MgONPs exert greater inhibitory effects on both enzymes than the leaf-derived counterpart, although their activity remained below that of the reference drug acarbose (Fig. 9). Samanta *et al.* (2025) synthesized silver nanoparticles using *Carica papaya* leaf extract, which showed MIC values of 20 µg/mL against *E. coli* and 30 µg/mL against *S. aureus*. Thus, nearly 90% inhibition of biofilm formation was achieved and minimal hemolytic and cellular toxicity up to 50 µg/mL was exhibited, highlighting their excellent antibacterial and antibiofilm performance.

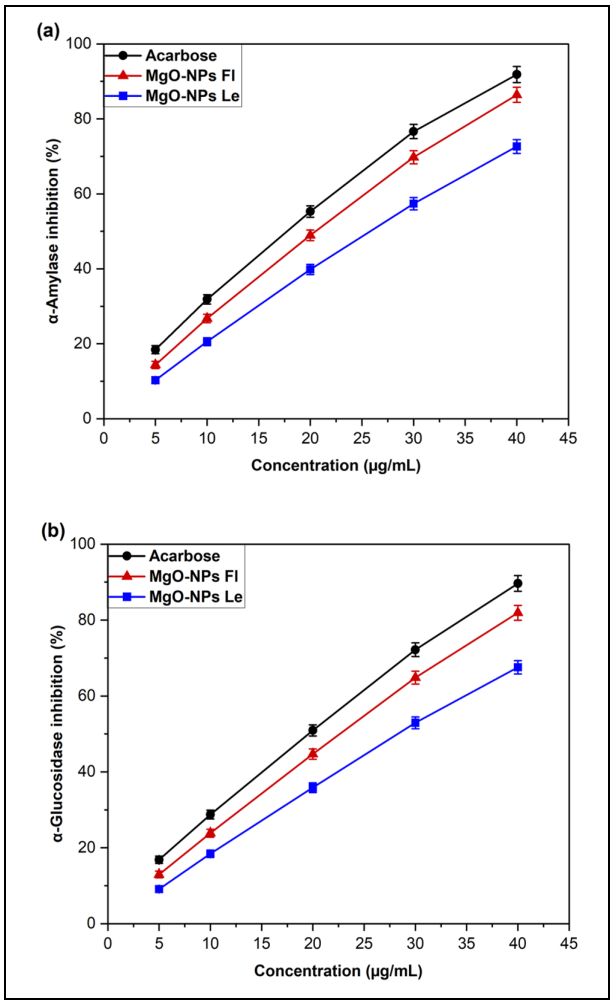


**Fig. 9: (a) α-Amylase and (b) α-Glucosidase inhibitory activity**

The inhibitory response of α-amylase increased with the concentration of both MgONPsFl and MgONPsLe (Fig. 9a). Enzyme suppression became progressively greater as the nanoparticle level was raised from 5 to 40 µg mL$^{-1}$. At the maximum concentration (40 µg mL$^{-1}$), acarbose produced the greatest inhibition (92.1%), followed by MgONPsFl (86.5%) and MgONPsLe (72.3%). The calculated $IC_{50}$ values were 18.9 µg mL$^{-1}$ for acarbose, 20.6 µg mL$^{-1}$ for MgONPsFl, and 27.8 µg mL$^{-1}$ for MgONPsLe, demonstrating that the flower-derived MgO nanoparticles were more efficient α-amylase inhibitors than the leaf-derived counterpart. A comparable trend was obtained for α-glucosidase

inhibition (Fig. 9b). Increasing the nanoparticle concentration from 5 to 40 µg $mL^{-1}$ resulted in a gradual enhancement of inhibitory activity, with the highest response recorded at 40 µg $mL^{-1}$. Under these conditions, acarbose achieved 89.2% inhibition, whereas MgONPsFl and MgONPsLe produced 81.4% and 67.6% inhibition, respectively. The corresponding $IC_{50}$ values were determined as 19.7 µg $mL^{-1}$ for acarbose, 22.9 µg $mL^{-1}$ for MgONPsFl, and 28.6 µg $mL^{-1}$ for MgONPsLe. These observations demonstrate that flower-derived MgO nanoparticles possess greater α-glucosidase inhibitory capacity than leaf-derived MgO nanoparticles, although both remain less effective than the reference drug acarbose.

### 3.2.4 Antimicrobial Action

Evaluation by agar well diffusion assay demonstrated that the biosynthesized magnesium oxide nanoparticles exerted pronounced antibacterial activity against examined Gram-positive and negative bacterial strains. In contrast, flower and leaf extracts did not produce detectable antibacterial effects at identical experimental conditions. None of the evaluated materials exhibited antifungal activity against either of two *Candida* species. The MgONPsFl generated wider inhibition zones than the MgONPsLe (Table 3).

The minimum inhibitory concentration and minimum bactericidal concentration analyses also substantiated the antimicrobial effectiveness of the biosynthesized MgO nanoparticles. A similar pattern was observed for the MBC measurements, further indicating that the flower-derived nanoparticles possessed enhanced bactericidal capability compared with the leaf-derived counterpart. In an earlier investigation, MgO nanoparticles prepared using watermelon peel extract produced inhibition zones of 23.7 ± 0.4 mm against *S. aureus* and 15.4 ± 0.25 mm against *E. coli*. Those nanoparticles also exhibited MIC values of 50–200 µg/mL, a DPPH $IC_{50}$ of 223 µg/mL, antiviral efficiencies of 84.7% against HAV and 49.7% against HSV-1 at 62.5 µg/mL, together with pronounced antibiofilm activity against MRSA (Selim *et al.* 2025b). The MBC/MIC ratios additionally demonstrate that both nanoparticle formulations possess bactericidal activity (Table 4).

**Table 3. Comparison of antimicrobial activity**

| Microorganisms Strains | Zone of Inhibition | | | | |
|---|---|---|---|---|---|
| | MgONPs Fl | MgONPsLe | Flowers Derived Fl | Leaves Derived Le | Standard |
| Bacterial Variant | | | | | Levofloxacin |
| *E. coli* ATCC 35218 | 14.8 ± 0.08[c] | 12.6 ± 0.10[d] | 0.0 ± 0.0 | 0.0 ± 0.0 | 28.5 ± 0.10[a] |
| *Enterococcus faecalis* ATCC 29212 | 14.3 ± 0.09[c] | 13.7 ± 0.08[c] | 0.0 ± 0.0 | 0.0 ± 0.0 | 25.4 ± 0.10[a] |
| *Staphylococcus epidermidis* CIP 106510 | 14.7 ± 0.07[c] | 13.8 ± 0.10[c] | 0.0 ± 0.0 | 0.0 ± 0.0 | 29.6 ± 0.12[a] |
| *Bacillus cereus* ATCC 14579 | 27.4 ± 0.15[b] | 20.3 ± 0.18[c] | 0.0 ± 0.0 | 0.0 ± 0.0 | 33.2 ± 0.11[a] |
| *Staphylococcus aureus* ATCC 43300 | 16.8 ± 0.12[b] | 13.4 ± 0.09[c] | 0.0 ± 0.0 | 0.0 ± 0.0 | 27.2 ± 0.15[a] |
| *Salmonella typhimurium* ATCC 14028 | 17.4 ± 0.10[b] | 15.3 ± 0.08[c] | 0.0 ± 0.0 | 0.0 ± 0.0 | 32.1 ± 0.09[a] |
| *Listeria monocytogenes* ATCC 19115 | 15.6 ± 0.09[c] | 12.9 ± 0.11[d] | 0.0 ± 0.0 | 0.0 ± 0.0 | 31.8 ± 0.08[a] |
| Fungal species | | | | | Amphotericin B (30 µg $mL^{-1}$) |
| *Candida krusei* | 0.0 ± 0.0 | 0.0 ± 0.0 | 0.0 ± 0.0 | 0.0 ± 0.0 | 15.4 ± 0.06[a] |
| *Candida albicans* | 0.0 ± 0.0 | 0.0 ± 0.0 | 0.0 ± 0.0 | 0.0 ± 0.0 | 18.2 ± 0.08[a] |

**Table 4. MIC–MBC antibacterial evaluation**

| Microorganism Strains | MgONPsFl (Mean ± SD) | | | MgONPsLe (Mean ± SD) | | |
|---|---|---|---|---|---|---|
| Bacterial strains | MIC | MBC | MBC/MIC | MIC | MBC | MBC/MIC |
| *Enterococcus faecalis* ATCC 29212 | 75 ± 0.09[c] | 150 ± 0.10[b] | 2 | 150 ± 0.12[b] | 300 ± 0.13[a] | 2 |
| *Salmonella typhimurium* ATCC 14028 | 75 ± 0.11[c] | 150 ± 0.09[b] | 2 | 150 ± 0.13[b] | 300 ± 0.10[a] | 2 |
| *Staphylococcus aureus* ATCC 43300 | 37.5 ± 0.08[d] | 75 ± 0.10[c] | 2 | 75 ± 0.12[c] | 150 ± 0.09[b] | 2 |
| *Bacillus cereus* ATCC 14579 | 37.5 ± 0.07[d] | 75 ± 0.08[c] | 2 | 75 ± 0.11[c] | 150 ± 0.09[b] | 2 |
| *Staphylococcus epidermidis* CIP 106510 | 37.5 ± 0.09[d] | 75 ± 0.08[c] | 2 | 75 ± 0.10[c] | 150 ± 0.12[b] | 2 |
| *Listeria monocytogenes* ATCC 19115 | 75 ± 0.10[c] | 150 ± 0.12[b] | 2 | 150 ± 0.09[b] | 300 ± 0.11[a] | 2 |
| *E. coli* ATCC 35218 | 75 ± 0.12[c] | 150 ± 0.08[b] | 2 | 150 ± 0.14[b] | 300 ± 0.10[a] | 2 |

**Table 5. Biofilm inhibition by MgONPs**

| Bacterial Variants | Biofilm Inhibition Percentage | |
|---|---|---|
| | Flower-Extracted MgONPsFl | Leaf-Extracted MgONPsLe |
| *Listeria monocytogenes* ATCC 19115 | 50.12[d] ± 0.03 | 37.24[f] ± 0.02 |
| *Staphylococcus epidermidis* CIP 106510 | 54.02[c] ± 0.05 | 47.18[e] ± 0.04 |
| *Enterococcus faecalis* | 45.08[e] ± 0.03 | 43.56[e] ± 0.02 |
| *E. coli* ATCC 35218 | 49.35[d] ± 0.02 | 38.62[f] ± 0.03 |
| *Staphylococcus aureus* | 63.48[a] ± 0.04 | 49.46[d] ± 0.03 |
| *Salmonella typhimurium* | 64.75[a] ± 0.03 | 33.16[f] ± 0.05 |
| *Bacillus cereus* | 58.46[b] ± 0.02 | 45.52[e] ± 0.03 |

The superior antibacterial activity of MgONPsFl compared with leaf-derived MgONPsLe may be attributed to differences in their physicochemical properties. MgONPsFl produced wider inhibition zones in both Gram-positive and negative bacterial species than MgONPsLe. This observation was consistent with the EDX results, which showed a higher magnesium atomic percentage in MgONPsFl (30.62 at%) than in MgONPsLe (29.03 at%), potentially contributing to the improved antibacterial response. Biofilm inhibition analysis also demonstrated enhanced activity for MgONPsFl, with inhibition values ranging from 45.08% to 64.75%, whereas MgONPsLe achieved 33.16%–49.46%. The maximum inhibition of biofilm formation by MgONPsFl was recorded against *Salmonella typhimurium* (64.75%) and *Staphylococcus aureus* (63.48%). In comparison, MgONPsLe produced lower inhibition across all evaluated bacterial strains, with values between 33.16% and 49.46% (Table 5).

#### 3.2.5 Mechanism of Antimicrobial Activity

The pronounced antibacterial performance of the flower-derived MgONPs against the evaluated bacterial species is likely associated with their greater lysozyme-like activity. Highest activity was recorded against *Bacillus cereus* and *Staphylococcus aureus*, reaching 47.28 and 46.62 AU $mL^{-1}$ $min^{-1}$, respectively. In comparison, the leaf-derived MgONPs produced lower corresponding values of 40.21 and 38.74 AU $mL^{-1}$ $min^{-1}$ (Table 6). This behavior may be attributed to the abundance of biologically active phytoconstituents in the flower extract, particularly those contributing to

lysozyme-like activity against *Bacillus cereus*. In addition, lipopolysaccharide degradation analysis demonstrated that both MgONPs effectively suppressed LPS production, with the extent of degradation varying among the tested bacterial species. The highest LPS degradation was detected for *Salmonella typhi*, reaching 61.45% for MgONPsFl and 58.46% for MgONPsLe, whereas low degradation percentages were observed for *Escherichia coli* (43.12% and 46.18%, respectively). Overall, these results demonstrate that both MgO nanoparticle formulations exert antibacterial effects through lysozyme-like activity and LPS degradation, with MgONPsFl consistently showing greater efficacy.

**Table 6. LPS and lysozyme-like degradation**

| Samples | Lysozyme Action (AU/mL/min) | | LPS Degradation (%) | |
|---|---|---|---|---|
| | *S. aureus* | *E. coli* | *E. coli* | *B. cereus* |
| MgONPsFI | 46.62 ± 0.03 | 43.12 ± 0.08 | 43.12 ± 0.08 | 47.28 ± 0.02 |
| MgONPsLe | 38.74 ± 0.04 | 46.18 ± 0.05 | 46.18 ± 0.05 | 40.21 ± 0.03 |

Flower-derived MgONPs possess a greater magnesium content than the leaf-derived counterpart. Their elevated MgO composition, together with a positively charged surface, promotes efficient electrostatic attraction toward negatively charged bacterial envelope components, including lipopolysaccharides in Gram-negative bacteria and teichoic acids in Gram-positive bacteria. These interactions weaken the cell envelope, enhance membrane permeability, and ultimately compromise bacterial integrity. Biosynthesized MgO nanoparticles commonly exhibit a positive surface potential that favors binding to the negatively charged LPS layer of bacterial membranes. Such attachment disrupts the structural organization of the membrane, increases its permeability, and enables MgO nanoparticles to interact with negatively charged biomolecules containing phosphorus and sulfur, resulting in membrane injury and structural deformation. The improved antibacterial performance of flower-derived MgONPs relative to leaf-derived MgONPs is also linked with variation in surface characteristics, MgO content, and particle morphology. The predominantly spherical morphology of MgONPsFl provides larger surface-area-to-volume, allowing more extensive contact by bacterial cells. Combined with their higher MgO content, these features contribute to enhanced antibacterial efficiency. Therefore, the superior antimicrobial activity of flower-derived MgONPs arises from the combined influence of their spherical morphology, favorable surface charge, and increased MgO content, which collectively strengthen interactions with and disruption of Gram-positive and negative bacterial membrane.

## 4. CONCLUSION

The present investigation reports a detailed synthesis of magnesium oxide nanoparticles through a plant-mediated approach employing aqueous leaf and flower extracts of *Vernonia elaeagnifolia*. This biosynthetic strategy offers an environmentally benign, reliable, and sustainable route for generating crystalline MgO nanomaterials possessing distinctive physicochemical and biological properties. Structural, morphological, and compositional characterization demonstrated that variations in elemental abundance and particle architecture, especially the rod and platelet-like nanostructures obtained from the flower- and leaf-derived samples, substantially influenced their biological responses. Both nanoparticle formulations displayed remarkable antioxidant, antidiabetic, and antimicrobial properties, confirming multifunctional bioactivity at evaluated *in vitro* experimental conditions. Flower-derived MgONPs consistently outperformed the leaf-derived counterpart, and this improved response is likely associated with their slightly greater magnesium content (30.62 at% compared with 29.03 at%) together with advantageous physicochemical features. Accordingly, flower-derived MgONPs achieved MIC values of 37.5–75 μg $mL^{-1}$, α-amylase and α-glucosidase $IC_{50}$ values of 21.5 and 22.9 μg $mL^{-1}$, and a maximum biofilm inhibition of 64.75%, demonstrating superior biological effectiveness relative to the leaf-derived nanoparticles. Collectively, these findings identify *Vernonia elaeagnifolia* as an efficient biological source for producing multifunctional MgONPs and as a renewable feedstock with considerable potential for sustainable nano pharmaceutical applications. Nevertheless, the current work is confined to *in vitro* biological evaluation and physicochemical characterization and therefore does not confirm *in vivo* therapeutic efficacy or safety. The incorporation of plant-derived phytochemicals into MgO nanostructures provides a sound platform for developing future therapeutic materials aimed at metabolic disorders, microbial diseases and oxidative stress. Further studies should include toxicological investigations and *in vivo* pharmacological, biocompatibility testing, and the development of *Vernonia elaeagnifolia*-based MgONP formulations for targeted delivery systems, including wound-healing nanogels and hydrogels, to establish their therapeutic and safety effectiveness before clinical translation.

## FUNDING

This research received no specific grant from any funding agency in the public, commercial, or not-for-profit sectors.

## CONFLICTS OF INTEREST

The authors declare that there is no conflict of interest.

## COPYRIGHT

This article is an open-access article distributed under the terms and conditions of the Creative Commons Attribution (CC BY) license (http://creativecommons.org/licenses/by/4.0/).

## REFERENCES

Al-Harbi, L. M., Ezzeldien, M., Elhenawy, A. A. and Said, A. H., Assessment of the bioactivity of bioinspired magnesium oxide nanoparticles from the Azadirachta indica extract, *Front. Bioeng. Biotechnol.,* 12, 1480694 (2024). https://doi.org/10.3389/fbioe.2024.1480694

Ali, S., Sudha, K. G., Thiruvengadam, M. and Govindasamy, R., Biocompatible synthesis of magnesium oxide nanoparticles with effective antioxidant, antibacterial, and anti-inflammatory activities using Magnolia champaca extract, *Biomass Convers. Biorefine.,* 14(17), 21431–21442 (2024). https://doi.org/10.1007/s13399-023-04252-3

Amina, M., Al Musayeib, N. M., Alarfaj, N. A., El-Tohamy, M. F., Oraby, H. F., Al Hamoud, G. A., Bukhari, S. I. and Moubayed, N. M. S., Biogenic green synthesis of MgO nanoparticles using *Saussurea costus* biomasses for a comprehensive detection of their antimicrobial, cytotoxicity against MCF-7 breast cancer cells and photocatalysis potentials, *PLoS One,* 15(8), e0237567 (2020). https://doi.org/10.1371/journal.pone.0237567

Ammulu, M. A., Vinay Viswanath, K., Giduturi, A. K., Vemuri, P. K., Mangamuri, U. and Poda, S., Phytoassisted synthesis of magnesium oxide nanoparticles from Pterocarpus marsupium rox.b heartwood extract and its biomedical applications, *J. Genet. Eng. Biotechnol.,* 19(1), 21 (2021). https://doi.org/10.1186/s43141-021-00119-0

Behera, K., Nasim, I. and Rajesh, K. S., Antioxidant and Anti-Inflammatory Activity of Magnesium Oxide Nanoparticles - an in Vitro Study, *Int. J. Dent. Oral Sci.,* 8(5), 2913–2917 (2021). https://doi.org/10.19070/2377-8075-21000568

Chandramohan, S., Ramalingam, P., Krishna, G. S., Manikandan, E. and Rajagopalan, R., Multifaceted investigation of zinc oxide nanoparticles synthesized from Vernonia elaeagnifolia leaf extract: Characterization, antibacterial, antioxidant, cytotoxicity, and DNA binding activities, *Inorg. Chem. Commun.,* 177, 114384 (2025). https://doi.org/10.1016/j.inoche.2025.114384

Chowdhury, L., Ebenezer, A. J. P., ShivaPrakash, S., Kirthiga, R., Mayakannan, S. and Subramaniam, M., Multi-objective optimization of heat-treated date palm seed biomaterials using genetic algorithms and Taguchi method, *Interact.,* 247(1), 179 (2026). https://doi.org/10.1007/s10751-026-02515-9

Devi, M. R. C. and Ramesh, B., Synthesis of Bougainvillea spectabilis Leaf Extract-mediated ZnO, MgO and CuO Nanoparticles, *J. Environ. Nanotechnol.* 15(1), 167–174 (2026). https://doi.org/10.13074/jent.2026.03.2521493

Elhawary, E. A., Soltane, R., Moustafa, M. H., Abdelaziz, A. M., Said, M. A. and Zahran, E. M., Sustainable $MnO_2$/MgO Bimetallic Nanoparticles Capped with Sword Fern Methanol Extract Attain Antioxidant/Anti-Biofilm Potential: A UPLC-ESI/LC/MS and Network Pharmacology-Supported Study, *Pharma.,* 18(9), 1262 (2025). https://doi.org/10.3390/ph18091262

Fahmy, N. F., Abdel-Kareem, M. M., Ahmed, H. A., Helmy, M. Z. and Mahmoud, E. A. R., Evaluation of the antibacterial and antibiofilm effect of mycosynthesized silver and selenium nanoparticles and their synergistic effect with antibiotics on nosocomial bacteria, *Microb. cell Fact.,* 24(1), 6 (2025). https://doi.org/10.1186/s12934-024-02604-w

Farzaneh, Z., Hanifian, H., Nateghpour, M., Hasanpour, G., Raeisi, A., Shabani, M., Farivar, L., Khezri, A., Dehdast, S. A. and Shahsavari, S., Antimalarial potential of Matricaria chamomilla-derived MgO nanoparticles against Plasmodium falciparum strains: an experimental study, *BMC Complement. Med. Therap.,* 25(1), 360 (2025). https://doi.org/10.1186/s12906-025-05081-9

Govindhraj, S. and Shanmugam, R., Evaluation of embryonic toxicology, antimicrobial, antiinflammatory, and antioxidant activity of the Equisetum arvense mediated Magnesium oxide nanoparticles, *Med. J. Malaysia.,* 80, 16–26 (2025).

Gupta, R. K., Saravanan, V., Manikandan, K., Shalom, N., Arun kumar, K. and Mayakannan, S., Fatigue, impact, and mechanical behavior of tamarind cellulose reinforced birch/Khusha grass fiber hybrid bio composites, *Interact.,* 247(1), 104 (2026). https://doi.org/10.1007/s10751-026-02445-6

Hamid, L. L., Hassan, M. H. and Obaid, A. S., Allium sativum extract mediate the biosynthesis of palladium nanoparticles as potential nanodrug for combating multidrug-resistant bacteria and wound healing, *Mater. Chem. Phys.,* 321, 129507 (2024). https://doi.org/10.1016/j.matchemphys.2024.129507

Kandavalli, S. R., Sundramurthy, V. P., Krishnasamy, V. D., Prasad, G. N. R., Kasi, U. K., Rajesh, S., Kumar, B. R., Selvaraju, M., Kadaikunnan, S. and Khaled, J. M., Bioresin based hybrid green composite preparation using Holoptelea integrifolia fibers reinforced by Ziziphus jujuba seed particles: a fuzzy logic assisted optimization of mechanical behaviour, *Zeitschrift für Physikalische Chemie,* 239(5), 747–772 (2025). https://doi.org/10.1515/zpch-2024-0837

Kongara, G., Tabassum, K. S., Sai Kalyani, Y. C., Sree, C. K. and Chitturi, K. ChM., Synthesis, Characterization and in vitro evaluation of Magnesium oxide Nanoparticles as Potential Anti-diabetic agents, *Res. J. Biotechnol.,* 20(4), 168–176 (2025). https://doi.org/10.25303/204rjbt1680176

Kurhade, P., Kodape, S., Junghare, K. and Wankhade, A., Green synthesis of MgO nanoparticles using the flower extracts of Madhuca longifolia and study of their morphological and antimicrobial properties, *Biomass Convers. Biorefine.,* 14(11), 11813–11827 (2024). https://doi.org/10.1007/s13399-022-03452-7

Muhaimin, M., Chaerunisaa, A. Y., Rostinawati, T., Amalia, E., Hazrina, A. and Nurhasanah, S., A Review on Nanoparticles of Moringa Oleifera Extract: Preparation, Characterization, and Activity, *Int. J. App. Pharm*., 15(4), 43–51 (2023). https://doi.org/10.22159/ijap.2023v15i4.47709

Mustafa, E. A., Hashem, A. E. G., Elhifnawi, H. N., Nada, H. G. and Khattab, R. A., One-pot biosynthesis of silver nanoparticles with potential antimicrobial and antibiofilm efficiency against otitis media–causing pathogens, *Eur. J. Clin. Microbiol. Infect. Dis.,* 40(1), 49–58 (2021). https://doi.org/10.1007/s10096-020-03920-w

Ramaprabha, K., Saravanan, P., Rajeshkannan, R. and Kumar, S. V., Bio- inspired synthesis of magnesium oxide nanoparticles from Acalypha indica: Anti-bacterial, anti-oxidant and toxicity study, *Sustainable Chemistry One World*, 5, 100048 (2025). https://doi.org/10.1016/j.scowo.2025.100048

Sahith, V. N., Jagadeesan, A. K. and Sruthi, V. S., Sustainable Development of Magnesium Oxide Nanoparticles Using Pterocarpus santalinus and Their Antimicrobial Activity, *J. Environ. Nanotechnol.* 14(2), 189–195 (2025). https://doi.org/10.13074/jent.2025.06.2521527

Samanta, S., Ahmed, R., Das, S., Banerjee, J., Bandyopadhyay, A., Maji, K., Ghosh, T. and Dash, S. K., Unveiling the antibacterial potency of phyto-stabilized silver nanoparticles against MDR uropathogens and exploration of its biocompatibility towards healthy blood cells, *Microbial Pathogenesis,* 206, 107822 (2025). https://doi.org/10.1016/j.micpath.2025.107822

Selim, S., Almuhayawi, M. S., Alruhaili, M. H., Tarabulsi, M. K., Saddiq, A. A., Elamir, M. Y. M., Amin, M. A. and Al Jaouni, S. K., Pharmacological applications and plant stimulation under sea water stress of biosynthesis bimetallic ZnO/MgO NPs, *Sci. Rep.,* 15(1), 5263 (2025a). https://doi.org/10.1038/s41598-025-87881-0

Selim, S., Soliman, M. K. Y., Almuhayawi, M. S., Alruhaili, M. H., Gattan, H. S., Saddiq, A. A., Hagagy, N., Alzahrani, A. J., Al Jaouni, S. K. and Salem, S. S., Green synthesis, characterization, molecular simulation, and in vitro biomedical application of magnesium oxide nanoparticles, *Plos one,* 20(9), e0332367 (2025b). https://doi.org/10.1371/journal.pone.0332367

Shahid, S., Ejaz, A., Javed, M., Mansoor, S., Iqbal, S., Elkaeed, E. B., Alzhrani, R. M., Alsaab, H. O., Awwad, N. S., Ibrahium, H. A., Fatima, U., Zaman, S. and Nazim Sarwar, M., The Anti-Inflammatory and Free Radical Scavenging Activities of Bio-Inspired Nano Magnesium Oxide, *Front. Mater.,* 9, 875163 (2022). https://doi.org/10.3389/fmats.2022.875163

Sharmila, A. and Selvaraj, C. I., Phyto-synthesized MgO nanoparticles using Scutia myrtina Kurz extract: Promising insights into photocatalytic degradation, antioxidant potential, cytotoxicity and toxicity assessment, *J. Mol. Struct.,* 1304, 137698 (2024). https://doi.org/10.1016/j.molstruc.2024.137698

Sherin, C. T. S., Jayakumar, T., Anitha, T. S., Hsia, C. W. and Sundarapandian, S. M., Synthesis of Gold Nanoparticles Using Leaf Extracts of *Pterospermum Canescens* and *Vernonia Elaeagnifolia*: Characterization, Platelet Aggregation and Cytotoxic Studies, *ChemistrySelect.* 9(38), e202402100 (2024). https://doi.org/10.1002/slct.202402100

Soliman, M. K. Y., Doghish, A. S., Hashem, A. H., Abdel-Maksoud, M., El-Dakroury, W. A., Alamri, A., Ebaid, H., Hasanin, M. S. and Saied, E., Novel trimetallic ($TiO_2$-MgO-Au) nanoparticles: Biosynthesis, characterization, antimicrobial, and anticancer activities, *Green Proce. Syn*., 14(1), 20250007 (2025). https://doi.org/10.1515/gps-2025-0007

Subbarao, E., Sharma, D., Singh, P., Gupta, R. K., Gayathri, B. and Mayakannan, S., Influence of $B_4C$ and $TiO_2$ fillers on mechanical and tribological performance of Canna indica/Curaua fiber reinforced hybrid composites with ANN prediction, *Interact*., 247(1), 148 (2026). https://doi.org/10.1007/s10751-026-02511-z

Touqeer, S., Abid, S., Saeed, M. A. and Dar, U. I., Antipyretic, Antidiabetic and Irritant studies on the Methanolic Extracts and Polyherbal Mixture of *Breynia disticha* J.R. Forst. and G. Forst. and *Vernonia elaeagnifolia* DC, *J. Pharm. Technol.,* 17(8), 3658–3662 (2024). https://doi.org/10.52711/0974-360X.2024.00570

Velsankar, K., Aravinth, K., Ana Cláudia, P.-S., Wang, Y., Ameen, F. and Sudhahar, S., Bio-derived synthesis of MgO nanoparticles and their anticancer and hemolytic bioactivities, *Biocatal. Agri. Biotechnol.,* 53, 102870 (2023). https://doi.org/10.1016/j.bcab.2023.102870

Wulandari, F., Sari, A. A., Hapsari, P. S., Aji, B. N. C., Adiningsih, M. U., Hidayatullah, M. H. and Umaroh, A. K., In Vitro Antioxidant Activity and Cytotoxic Effect of Ethanol Extract of Vernonia elaeagnifolia Leaves against Breast Cancer Cell Lines, *Trop. J. Nat. Prod. Res.,* 8(7), 7921–7925 (2024). https://doi.org/10.26538/tjnpr/v8i7.39%20